

Two-Dimensional Self-Assembly of Latex Particles in Wetting Films on Patterned Polymer Surfaces

Yujie Sun and Gilbert C. Walker*

Department of Chemistry, University of Pittsburgh, Pittsburgh, Pennsylvania 15260

Received: December 4, 2001

The 2D self-assembly of micrometer-size latex particles in wetting films on patterned poly(dimethylsiloxane) (PDMS) polymer surfaces was studied. The dynamics of these processes were directly observed using an integrated zoom microscope and CCD camera. The direct observations revealed the particles are transported inside or toward the grooves of the pattern in the region where the liquid film is appropriately thin, and the particles self-assembly inside the grooves is caused by a lateral capillary force. Mechanisms for particle transportation and self-assembly are discussed.

Introduction

Particles self-assemble on surfaces by design or accident. For example, photonic crystals with unusual periodicities and hence properties can be grown from textured surfaces whose patterns template a lattice structure.¹ Bulk synthesis of functionalized nanoparticles can be enhanced by using a smooth but chemically patterned surface to bring the particles into proximity, also allowing connections between them to be controlled. Particle assembly also occurs spontaneously upon introducing surfaces into physiological solutions. For example, cells, larvae, and spores distribute onto patterned surfaces in ways that may influence intercellular communication.² It is hoped that insight into the basic mechanism of particulate assembly in these multicomponent systems can be derived from the study of simple model systems, such as colloidal particles.

Approaches to 2D or 3D self-assembly of colloidal particles have exploited electrostatic interactions,^{3–5} external electric fields,^{6,7} covalent bonding,⁸ and capillary forces.^{9–11} Fabricating optical devices with colloidal particles can require control of particle size and position to create arrays of particles that are periodic. Natan et al.¹² first employed the idea of chemically binding to assemble colloidal particles in 2D, and this work was extended by Sato et al.,¹³ He et al.,^{8,14} and Zheng et al.¹⁵ Using different approaches, Yeh et al.⁶ and Trau et al.⁷ employed an electric field to induce pattern formation in colloid dispersions, and Mio et al.¹⁴ utilized optical trapping to make an array of colloidal particles.

In this study, we report efforts to develop an easier and more effective method to make colloidal particle patterns, and we discuss the mechanisms of 2D self-assembly of latex particles in wetting films on patterned polymer surfaces. In the Experimental Section, the materials, experimental apparatus, and procedures are introduced. In the Experimental Results and Discussion section, detailed observations of the dynamics and discussions of the mechanisms in those processes are reported. The last section provides a conclusion.

Experimental Section

1. Materials. Polybead carboxylate 914 nm microspheres (Polyscience Inc., 2.61% solids-latex) were used. The solutions

were prepared by diluting the original suspension to the desired concentrations with deionized water. The patterned polymer cells were prepared by casting a prepolymer (Sylgard 184 silicone elastomer) onto single-crystal silicon masters (Ted Pella, Inc.) and leaving it to cure for 2 days. After peeling off the polymer, one obtains a polymer cell with patterns at the bottom, providing a negative of the master, see Figure 1. The size of the generated cell was typically 5 mm × 5 mm, and the depth was 0.5 mm. The pattern that was examined had 2 μm wide and 500 μm deep grooves that crossed and encircled 8 μm square mesas. On the master, a broader marking line was written every 500 μm, which was useful for orienting the sample for light microscopy.

2. Apparatus. An integrated zoom microscope (10× objective, 2× TV camera tube, motorized zoom system, motorized focus, through-the-lens illumination) of a Dimension 3100 AFM (DI) system was employed to observe the self-assembly processes. A CCD camera and a camcorder were used in some cases to record data.

3. Procedures. Most of the experiments were done at room temperature and ~20% humidity. Before use, the polymer cells were oxidized with air plasma to make their surfaces hydrophilic. A VIC 500 (Electronics Corporation) at power level 8 (highest level 10 = 1800 W) for 2 min was used to generate a hydrophilic layer on the cell surface. It was found that the cells should be used soon after the oxidization because overnight the cells lose their hydrophilic layers. To observe the process of colloidal particle self-assembly in wetting films, about 12.5 μL (equal to the volume of the cell) of 0.1% latex suspension was added to the cell and left to dry. The 2D-motorized positioning station was used to move the cell, the Z-scanner was used to focus, and the zooming optics of the microscope were used to zoom in where interested, tracking the whole process. The video function was used to save pictures of the processes.

Experimental Results and Discussion

1. Observations of the Dynamics of the Self-Assembly Process. Using the apparatus described above, the dynamics of the self-assembly process were directly observed and recorded.

In the beginning, the cell was filled with the 0.1% latex suspension to create an approximately flat liquid surface. As

* To whom correspondence should be addressed.

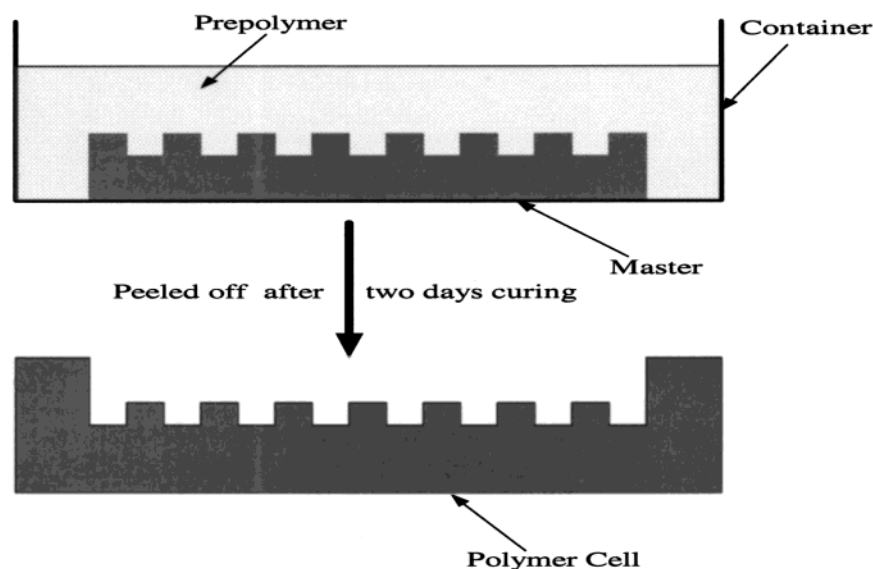


Figure 1. Preparation of the patterned polymer cells.

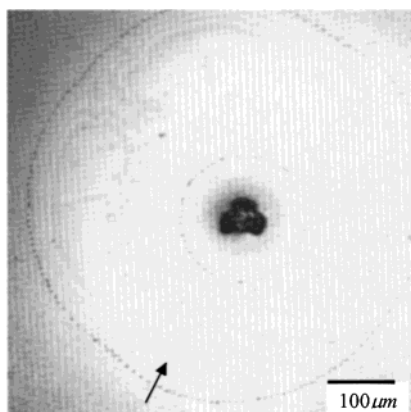


Figure 2. Dense colloidal particle array (about $50\ \mu\text{m}$ in diameter) which forms at the center of the cell when the thickness of the concave film center reduces to a value comparable with the size of the latex particles ($\sim 1\ \mu\text{m}$). Region A, rupture region (about $600\ \mu\text{m}$ in diameter) forms, as denoted by the arrow.

the water in the suspension evaporated, the liquid surface became concave because of the capillary force at the cell wall. At this stage, microscopic observations showed that the latex particles made Brownian motion, see Figure 1 in the Supporting Information. After the thickness of the concave center was reduced to a value comparable to the size of the latex particles ($\sim 1\ \mu\text{m}$), we observed a very small region (about $50\ \mu\text{m}$) at the center of the layer, containing particles that were more dense and ordered, see Figure 2 in the Supporting Information. As the film thinned, the wetting film at the center suddenly ruptured, leaving a dense particle array, and the periphery of the rupture region rapidly receded and formed a relatively dry region of about $400\text{--}600\ \mu\text{m}$ across. This characteristic region is hereafter denoted as region A, see Figure 2. The liquid film around the periphery of region A thickened because of film rupture and evolved into another dynamic equilibrium state. At this point, the process of pattern-assisted latex particle self-assembly started along the periphery of region A, see Figure 3a. The particles were transported toward to the leading edge of the pattern and moved inside the crossing grooves in directions both parallel and perpendicular to the direction of the net flux, see Figure 3 in the Supporting Information. The particles in the grooves were attracted to each other to form longer chains and crystals. The

patterned crystal grew radially toward the cell periphery. As more particles filled the grooves, a large beautiful pattern of colloid particle crystal formed, following the pattern of the substrate. At this point, there were no particles on the mesas. This characteristic region is hereafter denoted as region B, see Figure 3b. Microscopic observations showed that the flow rate of the particles significantly increased at a certain moment, and the rapidly moving particles self-assembled both on the mesas and in the grooves. This characteristic region is hereafter denoted as region C, see Figure 3c. The flow rate diminished during the formation of region C, and self-assembly only in grooves started again to form region B. In most cases, we observed that the radial formations of regions B and C occurred, see Figure 4 in the Supporting Information. In the whole process, because of the unevenness of the surface of the cell and some other factors such as polydispersity of colloid particles, air convection over the liquid film, surrounding conditions, motorized positioning station moving during observations, etc., the phenomena described above occurred with slight variations. For example, region A is rarely circular (Figure 2), although that would be expected because of surface tension, region C along the edge of region B does not necessarily exhibit a regular shape either, and the persistence of region C formation is not uniform across all areas, see Figure 4 in the Supporting Information. Some open spots can form in regions B and C, seen by Newton rings, and are caused by the local film rupture, see Figure 5 in the Supporting Information. We also used AFM to analyze the 2D latex particle patterned crystal formed by this process. The results are shown in Figure 4.

2. Discussion. *1. Mechanism of Particle Transportation.* The particles were brought to the growing pattern's edge by water flux. The question is, what makes this flux?

The system we are studying is an evaporating meniscus. Various authors^{17–20} have suggested that the pressure gradient in the liquid film is sufficient to support a fluid flow. Optical interferometry was used by them to obtain the meniscus profile, and resistance thermometry was used to obtain the heat flux for the evaporating meniscus. It was found that the different evaporation rates along the liquid–vapor interface result in the changes in the meniscus profile, which in turn results in a pressure gradient. An extended meniscus can be divided into three zones¹⁷ (see solid lines in Figure 5): (1) the immediate vicinity of the triple interline (junction of solid–liquid–vapor),

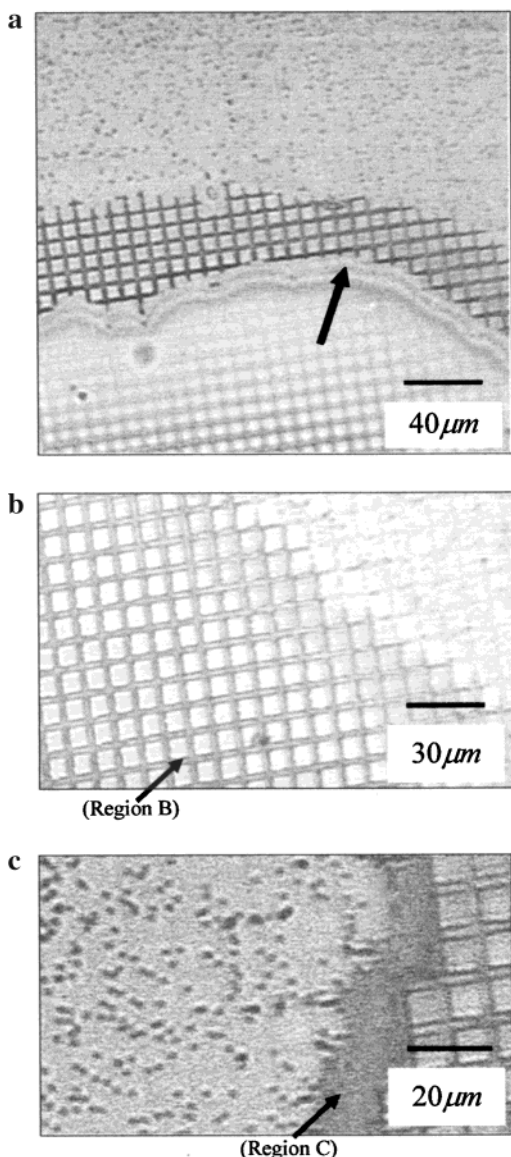


Figure 3. Several pictures of the late stage of the evaporation process (after the beginning of self-assembly in pattern). The square in each graph is $8 \mu\text{m} \times 8 \mu\text{m}$. (a) Pattern-assisted latex particle self-assembly starts along the periphery of region A, as denoted by the arrow. (b) A large beautiful pattern of colloid particle crystal forms, following the pattern of the substrate. (c) Particles self-assembling both on the mesas and in the grooves to form region C.

the thin film region, (2) the inner intrinsic meniscus region, and (3) the outer intrinsic meniscus region. Experimental and theoretical studies showed that the evaporation rate has a maximum at the transition point between the thin film region and the inner intrinsic meniscus region and decreases sharply to zero at the triple interline. The average flow rate $u(x)$ accordingly has the similar behavior, which is shown in Figure 5. For details about the pressure–gradient driven flow, see the Appendix.

Our observations of the particles' speeds close to the leading edge of the transition region (Figure 6a) can be used to test this model. As seen in Figure 5, in a minimal time period t , the meniscus interline recedes (because of evaporation) from 0 to x_0 with a rate V_M during region B formation. In this process, the film thickness at x_1 changes from h_0 to h_1 . We assume the contact angle is a constant and the average speed of the liquid flux $u(x)$ keeps the same profile along the meniscus. From the

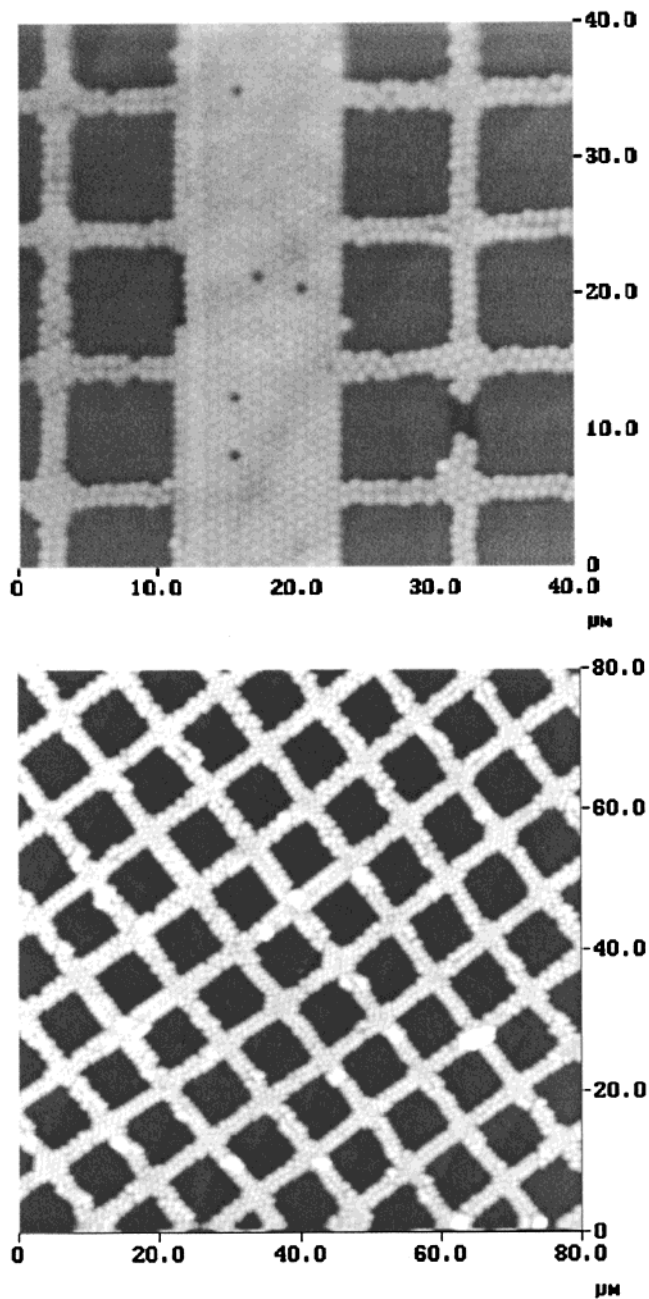


Figure 4. Height images of the formed 2D latex particle patterns (Dimension 3100 AFM, tapping mode).

similarity of the two meniscuses, we have

$$\frac{h_1}{h_0} = \frac{h(x_1 - x_0)}{h(x_1)} = \frac{x_1 - x_0}{x_1} = \frac{x_1 - V_M t}{x_1} \quad (1)$$

Hence

$$h(x_1 - x_0) = h(x_1) \left(1 - \frac{V_M t}{x_1} \right) \quad (2)$$

As shown in the appendix, the fluid flow rate is

$$u(x) = \frac{\int_0^{h(x)} u(y) dy}{\int_0^{h(x)} dy} = -\frac{\gamma_{lv} h(x)'''}{3\mu} h(x)^2 \quad (3)$$

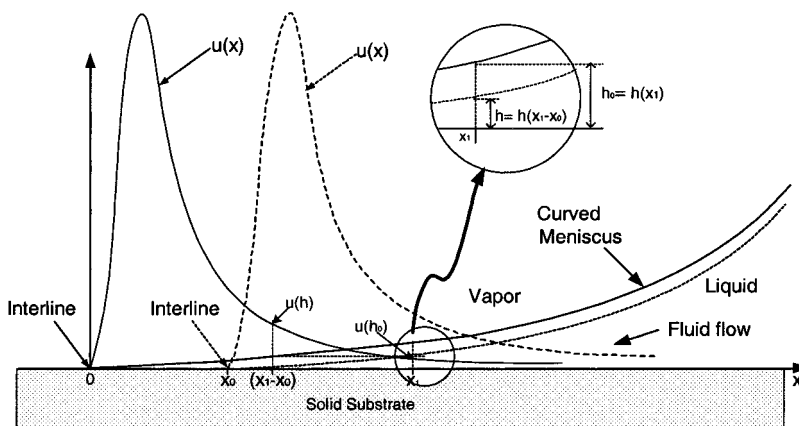


Figure 5. Evaporating meniscus and the average flow rate “ $u(x)$ ” distribution (solid lines). In a minimal time period t , the meniscus interline recedes from 0 to x_0 . The solid lines show the case where the meniscus interline is at 0, and the dashed lines show the case where the meniscus interline is at x_0 .

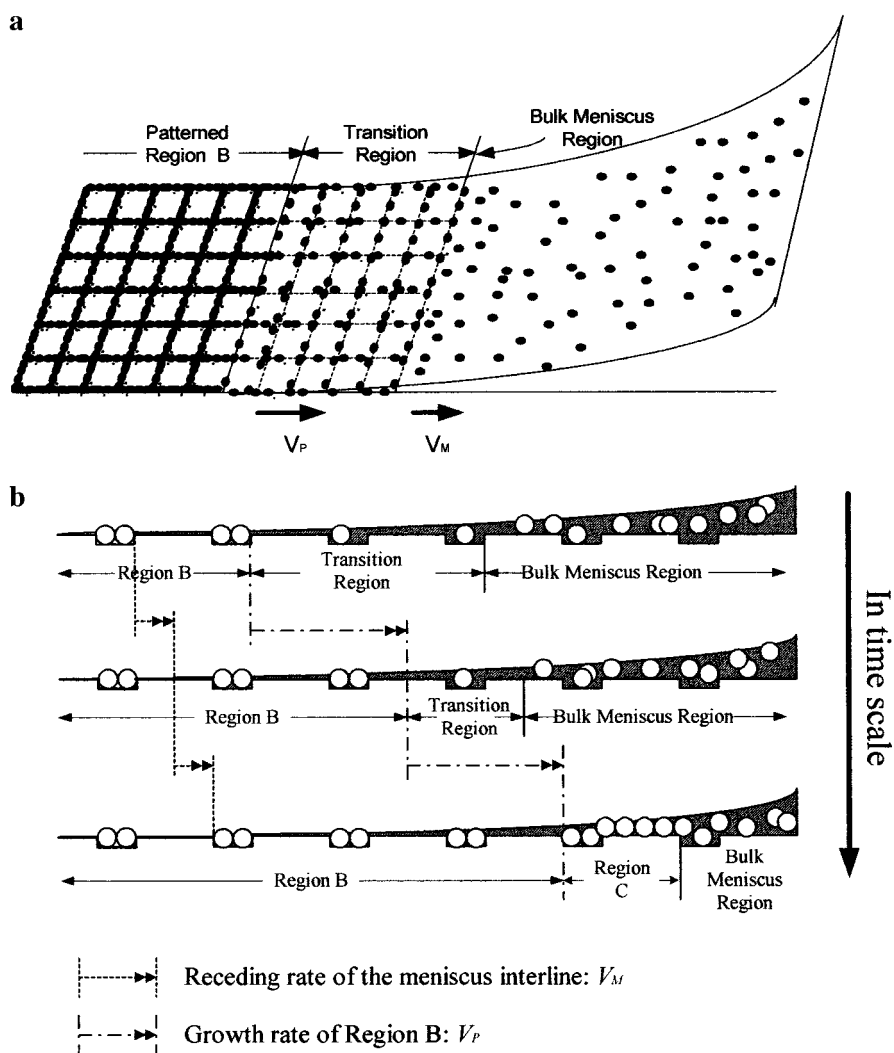


Figure 6. Formation of region C which is due to the competition between the pattern growth rate V_P and the meniscus receding rate V_M . (a) The competition between pattern growth rate V_P and the meniscus receding rate V_M causes the transition region to shrink. The square in the graph is $8 \mu\text{m} \times 8 \mu\text{m}$. (top view). (b) Cartoon illustrating relative changes of the transition region. Here, we suppose both V_M and V_P are constant and the shrinkage rate of the transition region equals $(V_P - V_M)$ (cross section view).

On the basis of the model in ref 17

$$h(x)''' = \frac{d^3 h(x)}{dx^3} = -\frac{3\mu\dot{n}^*}{\gamma_{lv}} \frac{1}{(h(x) + \delta^*)^3} \quad (4)$$

In (3) and (4), γ_{lv} is the surface tension, μ is the absolute viscosity, \dot{n}^* is the total incoming volumetric flow rate per unit width, which is a constant, and the parameter δ^* is a measure of the region over which evaporation occurs and of the size of the initial pressure gradient in the model. Combining (3) and

(4), one obtains

$$u(x) = -\frac{\gamma_{lv}h(x)''''h(x)^2}{3\mu} = \dot{n}^* \frac{h(x)^2}{(h(x) + \delta^*)^3} \quad (5)$$

The region that we are studying is part of the bulk meniscus region (Figure 6a,b) which is close to the transition region leading edge. In this region, the film thickness is slightly larger than the particle size ($1 \mu\text{m}$) and the particles are dragged by the fluid flow. Within this range of film thickness, the fluid flow is laminar and viscous. The speed of the particle should be proportional to the flow rate. Therefore, one obtains

$$v(x) = A^*u(x) \quad (6)$$

where $v(x)$ is the speed of the particle, A is the proportional coefficient, and $u(x)$ is the flow rate. Thus, after introducing (2) and (5) into (6)

$$v(t)_{x_1} = v(h) = A\dot{n}^* \frac{h(x_1 - x_0)^2}{(h(x_1 - x_0) + \delta^*)^3} \quad (7)$$

For the simplicity of the discussion, in the region we are studying (relatively far from the interline), we assume a constant volumetric flow rate in this evaporating meniscus, which is according to the parameter $\delta^* = 0$. Thus (7) becomes

$$v(t)_{x_1} = v(h) = A\dot{n}^* \frac{1}{h(x_1 - x_0)} \quad (8)$$

From (2) and (8), one gets

$$\begin{aligned} v(t)_{x_1} = v(h) &= A\dot{n}^* \frac{1}{h(x_1 - x_0)} = A\dot{n}^* \frac{1}{h(x_1) \left(1 - \frac{V_M t}{x_1}\right)} \\ &= v(t=0)_{x_1} \frac{1}{1 - \frac{V_M t}{x_1}} \end{aligned} \quad (9)$$

To test the above model, we collected data from video of the process, as follows.

We chose an area that is close to the leading edge of the transition region and measured the average speeds of five different particles found within $100 \mu\text{m}$ of each other. We sampled over this area to reduce the influence of factors other than the fluid flow rate. (The data collected are shown in the Supporting Information).

We plotted the average speed versus time and fitted a reciprocal function as follows, see Figure 7:

$$v(t)_{x_1} = a \frac{1}{1 - bt} = 5.00 \frac{1}{1 - 0.017t} \quad (10)$$

The fitting yields $a = 5.00 \mu\text{m/s}$ and $b = 0.017 \text{ s}^{-1}$. The value of a is close to the coefficient " $v(t=0)_{x_1} = 4.93 \mu\text{m/s}$ " in (9).

We have estimated the value of the parameter V_M/x_1 as follows: The motion of the transition region leading edge provides V_M . From the first two pictures in Figure 6 of the Supporting Information, the transition region leading edge moved about $14 \mu\text{m}$ in 15 s . Thus, V_M can roughly be $14 \mu\text{m}/15 \text{ s}$. We know $x_1 = 48 \mu\text{m}$; hence, $V_M/x_1 = (14/15)/48 = 0.019 \text{ s}^{-1}$. This parameter is also very close to the corresponding parameter from the numerical fit, reported above. The quality of the fit to the data supports the use of this transportation model.

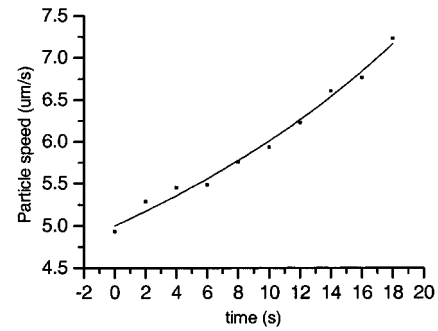


Figure 7. Average speed $v(t)$ ($\mu\text{m/s}$) that changes with time (s) at a fixed point. The data were fitted with a reciprocal function. The error of the measurement is about the size of the points.

Why does region C form, where one sees dense packing of particles on grooves AND mesas? We propose the following model, where the liquid film thickness determines particle mobility, see Figure 6a,b. When region B forms, the particles move only within either parallel or perpendicular grooves of the transition region; there is inadequate flow atop the mesas. On the other hand, in the bulk meniscus region, flow atop the entire surface is strong enough that particles glide over the grooves and fail to fill them. As region B grows, the transition region shortens, see Figure 6 in the Supporting Information. Finally it disappears, and region B directly contacts the bulk meniscus region. Region C starts to form because the film thickness at the interline is now close to $1 \mu\text{m}$. This dynamic process is illustrated by a cartoon in Figure 6b. Because the contact angle is a constant, we conclude that the rate of region B's growth, V_P , is greater than the rate the meniscus interline to recede, V_M , because of evaporation. Region C grows more slowly than region B because region C requires many more particles per unit area. V_M exceeds V_P , causing the film thickness of the vicinity of the interline to be reduced until a transition region appears. At this point, region B reforms (see Figure 4 of Supporting Information). Other factors, including large size particles, higher features of the substrate, coagulation of the particles, and the contact line pinning effect,^{21,22} can lead to the formation of localized C-type regions, which depends on the film thickness close to the pattern's leading edge. (See Figure 4 of the Supporting Information.)

2. Mechanism of the Self-Assembly. We return to the region of crystal formation. There is a wetting film in this region. In region B, microscopic observations show that, in the transition region, the particles move inside the grooves in either parallel or perpendicular directions, and finally forward to the leading edge of region B. As they move inside the grooves, the particles self-assemble. The incoming particles either incorporate into an existing crystal or form new short chains, which then attract each other to form longer chains. Previous work by Kralchevsky et al.²³⁻²⁵ and Yamaki et al.²⁶ has shown that the lateral capillary force drives self-assembly in a similar situation. A lateral capillary force exists between the particles partially immersed in a liquid layer. The deformation of the liquid layer because of the wetting of the particle surface provides the lateral capillary force,^{11,23-26} see Figure 8. Self-assembly in the grooves perpendicular to the flux direction strongly supports that the lateral capillary force is acting on the partially immersed particles. Apparently, the presence of the transition region just allows the action of the lateral capillary force.

Conclusion

In this study, the bottom-patterned polymer cells were made and used to study the process of the two-dimensional self-

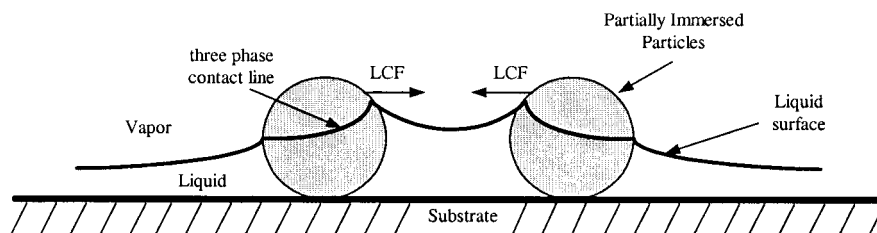


Figure 8. Physical nature of the lateral capillary force (LCF) between the partially immersed particles. The LCF is the total effect of the vapor pressure, liquid pressure, and the surface tension along the three phase contact line on the particles.

assembly of latex particles in wetting films on patterned surfaces. On the basis of direct microscopic observations, the mechanisms of the particle transportation and the particle self-assembly were discussed. The particles were transported by a flux caused by the pressure gradient in an evaporating meniscus. The self-assembly of particles was driven by the lateral capillary force between the partially immersed particles. 2D latex particle patterned crystals can be designed by exploiting the features of the substrate.

This paper has demonstrated a method to generate 2D latex particle patterns over a spatial range of up to 200 μm . An important future direction of this work is to extend uniform patterning over several millimeters. This is necessary for constructing photonic devices of practical dimensions. In addition, patterning of biological particles using this technique, in varying solvents and with particles of different modulus, should also prove possible. This may also provide insight into the design of textured polymer surfaces for applications such as nontoxic, fouling prevention in marine and implant environments.

Acknowledgment. We gratefully acknowledge the Office of Naval Research (N00014-96-1-0735), National Science Foundation (Grant NSF-9816820), and Army Research Office (16-99-C-1036) for financial support. G.C.W. thanks 3M Company for an Untenured Faculty Award.

Appendix

Fluid Flow Driven by the Pressure Gradient Due to Curvature in an Evaporating Meniscus. The local liquid film pressure is related to the ambient pressure by capillary equation

$$P_v - P_l(x) = \gamma_{lv}K(x) \quad (\text{A1})$$

where $K(x)$ is the local curvature of the liquid–vapor interface and γ_{lv} is the surface tension. A change in curvature then provides a mechanism for producing the pressure gradient for flow in the evaporating meniscus. Assuming constant surface tension along the interface, eq 1 can be differentiated as follows:

$$-\frac{dp_l}{dx} = \gamma_{lv} \frac{d}{dx} \left[\frac{h''}{(1+h'^2)^{3/2}} \right] = \gamma_{lv} \left[h'''' - \frac{3}{2} h' h''^2 + \Lambda \right] \quad (\text{A2})$$

It has been common practice to ignore all terms except for the first in the interline vicinity because of the small meniscus slope. Thus (A2) becomes

$$-\frac{dp_l}{dx} = \gamma_{lv} h'''' \quad (\text{A3})$$

The Navier–Stokes momentum equation gives

$$\frac{dp_l}{dx} = \mu \frac{d^2 u}{dy^2} \quad (\text{A4})$$

where μ is the viscosity coefficient. Solving (A3) and (A4) under the appropriate no-slip condition at $y = 0$ and no-shear condition at $y = h$, one obtains

$$u(y) = \frac{-\gamma_{lv} h''''}{\mu} \left(\frac{y^2}{2} - hy \right) \quad (\text{A5})$$

and

$$u(x) = \frac{\int_0^{h(x)} u(y) dy}{\int_0^{h(x)} dy} = -\frac{\gamma_{lv} h'''' h^2}{3\mu} \quad (\text{A6})$$

It is not possible to obtain the analytical solutions to the above equations. However, by experimentally and theoretically studying the evaporating meniscus, various authors have found that the evaporation rate has its maximum close to the interline caused by the local temperature difference between the liquid–vapor interface and substrate surface.

Supporting Information Available: Figures 1–6 and Table 1. This material is available free of charge via the Internet at <http://pubs.acs.org>.

References and Notes

- (1) van Blaaderen, A.; Ruel, R.; Wiltzius, P. *Nature* **1997**, *385*, 321.
- (2) van Blaaderen, A.; Wiltzius, P. *Adv. Mater.* **1997**, *9*, 833.
- (3) Andersson, M.; Berntsson, P.; Jonsson, P.; Gatenholm, P. *Biofouling* **1999**, *14*, 167–178.
- (4) Roberts, C.; Chen, S. C.; Mrksich, M.; Martichonok, V.; Ingber, E. D.; Whitesides, G. M. *J. Am. Chem. Soc.* **1998**, *120* (26), 6548–6555.
- (5) Chen, K. M.; Jiang, X.; Kimerling, L. C.; Hammond, P. T. *Langmuir* **2000**, *16*, 7825–7834.
- (6) Tien, J.; Terfort, A.; Whitesides, G. M. *Langmuir* **1997**, *13*, 5349–5355.
- (7) Schmitt, J.; Machtle, P.; Eck, D.; Mohwald, H.; Helm, C. A. *Langmuir* **1999**, *15*, 3256.
- (8) Yeh, S.; Seul, M.; Shraiman, B. I. *Nature* **1997**, *386*, 57–59.
- (9) Trau, M.; Saville, D. A.; Aksay, I. A. *Science* **1996**, *272*, 706–709.
- (10) Trau, M.; Sankaran, S.; Saville, D. A.; Aksay, I. A. *Nature* **1995**, *374*, 437–439.
- (11) Hayward, R. C.; Saville, D. A.; Aksay, I. A. *Nature* **2000**, *404*, 56–59.
- (12) He, H. X.; Zhang, H.; Li, Q. G.; Zhu, T.; Li, S. F. Y.; Liu, Z. F. *Langmuir* **2000**, *16*, 3846–3851.
- (13) Jiang, P.; Bertone, J. F.; Hwang, K. S.; Colvin, V. L. *Chem. Mater.* **1999**, *11*, 2132–2140.
- (14) Dushkin, C. D.; Nagayama, K.; Miwa, T.; Kralchevsky, P. A. *Langmuir* **1993**, *9*, 3695–3701.
- (15) Denkov, N. D.; Velev, O. D.; Kralchevsky, P. A.; Ivanov, I. B.; Yoshimura, H.; Nagayama, K. *Nature* **1993**, *361*, 26.
- (16) Freeman, R. G.; Grabar, K. C.; Allison, K. J.; Bright, R. M.; Divas, J. A.; Guthrie, A. P.; Hommer, M. B.; Jackson, M. A.; Smith, P. C.; Walter, D. G.; Natan, M. J. *Science* **1995**, *267*, 1629–1632.
- (17) Sato, T.; Hasko, D. G.; Ahmed, H. *J. Vac. Sci. Technol. B* **1997**, *15*, 45.
- (18) He, H. X.; Huang, W.; Zhang, H.; Li, Q. G.; Li, F. Y. S.; Liu, Z. F. *Langmuir* **2000**, *16*, 517.
- (19) Zhang, J.; Zhu, Z.; Chen, H.; Liu, Z. *Langmuir* **2000**, *16*, 4409–4412.
- (20) Mio, C.; Marr, D. W. M. *Adv. Mater.* **2000**, *12*, 917.
- (21) Renk, F. J.; Wayner, P. C., Jr. *J. Heat Transfer* **1978**, *101*, 55–62.

- (18) Moosman, S.; Homsy, G. M. *J. Colloid Interface Sci.* **1980**, *73*, 212–223.
- (19) Renk, F. J.; Wayner, P. C., Jr. *J. Colloid Interface Sci.* **1978**, *67*, 408–414.
- (20) Potash, M., Jr.; Wayner, P. C., Jr. *Int. J. Heat Mass Transfer* **1972**, *15*, 1851–1863.
- (21) Deegan, R. D.; Bakajin, O.; Dupont, T. F.; Huber, G.; Nagel, S. R.; Witten, T. A. *Nature* **1997**, *389*, 827.

- (22) Deegan, R. D.; Bakajin, O.; Dupont, T. F.; Huber, G.; Nagel, S. R.; Witten, T. A. *Phys. Rev. E* **2000**, *62*, 756–765.
- (23) Kralchevsky, P. A.; Nagayama, K. *Adv. Colloid Interface Sci.* **2000**, *85*, 145–192.
- (24) Dushkin, C. D.; Nagayama, K.; Miwa, T.; Kralchevsky, P. A. *Langmuir* **1993**, *9*, 3695.
- (25) Kralchevsky, P. A.; Nagayama, K. *Langmuir* **1994**, *10*, 23.
- (26) Yamaki, M.; Higo, J.; Nagayama, K. *Langmuir* **1994**, *10*, 432.